

Modeling of streamer-to-spark transitions in the first pulse and the post discharge stage

Xiancong Chen¹ , Yifei Zhu^{1,2}  and Yun Wu^{1,2} 

¹ Science and Technology of Plasma Dynamics Laboratory, Airforce Engineering University, Xi'an 710038, People's Republic of China

² Institute of Aero-engine, School of Mechanical Engineering, Xi'an Jiaotong University, Xi'an 710049, People's Republic of China

E-mail: yifei.zhu.plasma@gmail.com and wuyun1223@126.com

Received 3 April 2020

Accepted for publication 29 April 2020

Published 9 September 2020



CrossMark

Abstract

The streamer-to-spark transition in a point-to-plane configuration in atmospheric pressure air is studied using a 2D–0D combined approach. A validated fluid code is used and improved to model the spark stage. 2D modeling of discharges at three different temperatures, 300, 600 and 800 K, are conducted; the spark transition occurs when the temperature reaches 800 K in the first pulse. A conservative criteria of spark transition temperature is proposed based on analytical solution and compared with experiments. Kinetics modeling of the post discharge stage is conducted with consistent input values extracted from the 2D model. Results show that the streamer-to-spark transition can be initiated at a lower temperature (600 K) and lower field (50–75 Td), and the long-lifetime O-atoms formed in previous pulses play an important role in ‘knocking off’ the electrons from negative charged species and maintaining the electron density in the post discharge stage. The dominating processes for electron production are electron detachment reactions from O_3^- , O_2^- and O^- . The ionizations from excited species only accelerate the production of electrons when the plasma is already dense.

Keywords: point-to-plane discharge, streamer, spark, fluid modeling

(Some figures may appear in colour only in the online journal)

1. Introduction

Electrical discharges generated in point-to-plane or point-to-point configurations are plasma sources widely used and studied in the fields of combustion/ignition [1–5], energy transition and fuel reforming [6–9], materials processing technology [10, 11], high voltage switches design [12] *et al.* By applying high voltage pulses on a point electrode, a streamer will form and propagate along the electric field line toward another electrode. Once the streamer touches the end (usually in the time scale of tens to hundreds of nanoseconds), the discharge will decay, or transit to a spark with a sharp increase of plasma density and deposited energy. To allow flexible control of plasma sources in above fields, deeper understandings of the mechanism of streamer-to-spark transitions are required.

The early studies of the atmospheric pressure air breakdown mechanism appeared several decades ago [13], and the theory of the streamer breakdown and the mechanism of the electric spark was introduced by Loeb and Meek [14, 15] in the middle of the 20th century. Detailed investigations of steamer breakdown mechanisms, streamers and their propagation have continued through intensive experimental and numerical studies [16–18] since then. Three possible mechanisms are responsible for steamer-to-spark transition: an attachment control process, chemical and stepwise ionization and gas density decrease. These mechanisms induce the streamer-to-spark transition by balancing the electron loss process and finally accelerating the ionization processes. A pioneering numerical study of the streamer-to-spark transitions can be found in [19], where a 1D approximation model and a 0D kinetics model are used, and the author concludes that the major cause of a spark

formation in a nanosecond timescale ($<1 \mu\text{s}$) was an increasing detachment rate due to the accumulation of oxygen atoms and other active particles.

Detailed experiments on point-to-point discharges have been carried out by Pai *et al* [20]. The nanosecond repetitively pulsed (NRP) discharges in atmospheric pressure air at the temperatures ranging from 300 to 1000 K were studied. The corona, glow, and spark regimes were identified based on gas temperature and electron density. An analytical model was proposed to explain the glow-to-spark transition, the NRP heating process was simplified to be a continuous heating process with a time-averaged volumetric power. Their model showed that the glow-to-spark transition was caused by the thermal ionization instability and the transition occurred at a certain reduced electric field $(E/N)_{\text{GS}}$ (144 Td). During the discharge, the gas density in the discharge channel reduced due to gas temperature rise, thus lower applied voltage was required for achieving $(E/N)_{\text{GS}}$.

A recent cycle of papers by Janda *et al* [21–26] presented the experimental measurements of transient sparks (TS) in the point-to-plane configurations. The cross-correlation spectroscopy technique was used to capture the streamer-to-spark transition [26], the results showed that the transition can happen either in the first pulse with a high voltage or after a chain of lower voltage pulses with a repetition rate of 8–10 kHz. Factors responsible for the transition were supposed: gas heating, accumulation of species such as atoms from the previous TS pulses, as well as generation of charged particles by stepwise ionization, but the role of each factors in the formation of spark is not revealed yet.

Impressive numerical investigations can be found in references [27, 28]. The dynamics of air discharges between two point electrodes in air at atmospheric pressure for two different gas temperatures 300 and 1000 K was studied. Simulation results showed that in the early stages of the glow regime, two opposite streamer discharges propagate in the gap and form a conductive channel between electrodes. After the connection of two opposite streamers, the electric field in the plasma channel between two electrodes becomes rather uniform and equals the average electric field (i.e. the applied voltage divided by gap distance). If the value of the average electric field is higher than the breakdown field in air (≈ 120 Td), the electron density continues increasing and the glow-to-spark transition may occur in the first pulse.

Despite the achievements in the researches of streamer-to-spark transition (especially in point-to-point configurations), there are very few works devoting to the streamer-to-spark transition after two electrodes is bridged by plasmas in a point-to-plane configuration. One of the reasons is that once the streamer head touch the cathode plane, the high electric field near the cathode and sharp increase of electron density in the channel lead to code crash or extremely small time step ($\sim 10^{-15}$ s) due to the decrease of dielectric relaxation time.

In this paper a 0D–2D combined modeling approach is used to study the formation and evolution of streamers and sparks in a point-to-plane configuration. The code is validated by existing experimental data. The role of gas temperature for spark

formation in the first pulse, and the kinetics contribution to the spark formation in the post discharge stage are studied.

2. Model description

The 2D PASSKEy (PArallel Streamer Solver with KinETics) code is used. The code was used in modeling of nanosecond surface discharges [29–31] and validated by measured discharge morphology, propagation velocity, voltage–current curves of experiments, and by a point-to-plane model benchmark [32]. Detailed mathematical formulations and validations can be found in paper [29, 31]. In this section we briefly present the equations solved, and introduce the modifications to the code for the transition and the spark phase. The widely used 0D modeling global plasma chemistry code ZDPlasKin [33, 34] is also used.

2.1. Model for the streamer phase

Drift-diffusion-reaction equations for species, Poisson equation for electric field, Helmholtz equations for photoionization and Euler equations for fluid dynamics are coupled. The drift-diffusion-reaction equations are:

$$\frac{\partial n_i}{\partial t} + \nabla \cdot \Gamma_i = S_i + S_{\text{ph}}, \quad i = 1, 2, \dots, N_{\text{total}} \quad (1)$$

$$\Gamma_i = -D_i \nabla n_i - (q_i/|q_i|) \mu_i n_i \nabla \Phi, \quad i = 1, 2, \dots, N_{\text{charge}} \quad (2)$$

where Φ is the electric potential, n_i , q_i , and S_i is the number density, charge and source function for species i , respectively. The source function S_i includes production and loss terms due to gas phase reactions and is calculated with detailed kinetics, and the kinetics scheme used in this paper has been validated in [29, 30], S_{ph} is the photoionization source term for electrons and oxygen ions. D_i and μ_i are the diffusion coefficients and mobility of charged species, the electron swarm parameters and the rate coefficients of electron impact reactions are represented as explicit functions of the reduced electric field E/N based on local field approximation (LFA). The diffusivity and mobility for ions and other charged heavy species are founded from experimental data [35]. In the code, $\nabla \cdot \Gamma_i = 0$ for neutral species is postulated. N_{total} and N_{charge} are the number of all species and charged species, respectively.

Photoionization affects the propagation and morphology of the volumetric streamer. An efficient photoionization model based on three-exponential Helmholtz equations [36, 37] is used to calculate S_{ph} . We assume that the photoelectrons come from the ionization of oxygen molecules by VUV-radiation coming from electronically excited N_2 in $b^1\Pi_u$, $b^1\Sigma_u^+$, $c^1\Sigma_u^+$ states [38].

The Poisson equation is solved for the entire computational domain:

$$\nabla(\varepsilon_0 \varepsilon_r \nabla \Phi) = - \sum_{i=1}^{N_{\text{ch}}} q_i n_i \quad (3)$$

where ε_0 is the permittivity of vacuum space and ε_r the relative permittivity of air, ε_r is assumed to be 1.0 in this paper. The electric field is obtained through $\mathbf{E} = -\nabla \Phi$.

Euler equations are solved for fluid dynamics, mainly for the gas temperature and density variations:

$$\frac{\partial \mathbf{U}}{\partial t} + \frac{\partial \mathbf{F}}{\partial x} + \frac{\partial \mathbf{G}}{\partial y} = \mathbf{S} \quad (4)$$

$$\mathbf{U} = \begin{bmatrix} \rho \\ \rho u \\ \rho v \\ e \end{bmatrix}, \mathbf{F} = \begin{bmatrix} \rho u \\ p + \rho uu \\ \rho uv \\ (e + p)u \end{bmatrix}, \mathbf{G} = \begin{bmatrix} \rho v \\ \rho vw \\ p + \rho vv \\ (e + p)v \end{bmatrix}, \mathbf{S} = \begin{bmatrix} 0 \\ 0 \\ 0 \\ S_{\text{heat}} \end{bmatrix} \quad (5)$$

where ρ is the total density of air, u and v are the velocities in 2 dimensions, and e is the specific total energy. The reactive Euler equations are closed by the equation of state:

$$p = (\gamma - 1) \rho i \quad (6)$$

where $i = e - (u^2 + v^2) / 2$ is the specific internal energy, γ is the specific heat ratio and equals to the ratio of the specific heat capacity at constant pressure C_p to the specific heat capacity at constant volume C_v .

The conductive current I and the total heat source S_{heat} is calculated by $I = \int_{\Sigma} \mathbf{j}_c \cdot d\Sigma$ and $S_{\text{heat}} = \mathbf{j}_c \cdot \mathbf{E}$, respectively, where \mathbf{j}_c is the conductive current density and Σ is the surface of the metallic anode. The calculated density, pressure and temperature from Euler equations are in turn used to update reduced electric field, Helmholtz equations and kinetics, the plasma-fluid coupling strategy has been illustrated in detail in paper [31].

In this work, the streamer dynamics at 300, 600 and 800 K are solved by a 2D fluid model without Euler equations, because in the short discharge timescale (60 ns in this work), the change of gas density and E/N due to fast gas heating is negligible [27, 28]. But to evaluate the influence of gas density variation due to temperature increase for further studies, a specific case fully coupling the drift-diffusion-reaction equations and the Euler equations is conducted, and the results are shown and discussed in figure 11.

2.2. Model for the spark phase

The model for the spark phase in the discharge in a point-to-point configuration has been studied in paper [27, 28]. After the connection of two opposite streamers, the electric field in the conductive plasma channel becomes relatively uniform and equals the average electric field (the potential difference between two electrodes divided by the gap distance). If the value of the average electric field is higher than the air breakdown field (about 120 Td) at atmospheric pressure, the electron density would continue to increase and the discharge transits to the spark. The rapid increase of the electron density and current makes the dielectric relaxation time δt_D become very small ($-10^{-15} \sim 10^{-16}$ s), resulting in a strong limitation on the time step. To treat this numerical problem, the authors of paper [28] ‘freeze’ the electric field distribution after the formation of conductive plasma channel and make the absolute value of electric field proportional to the applied voltage. This approach significantly accelerates the simulation with acceptable accuracy.

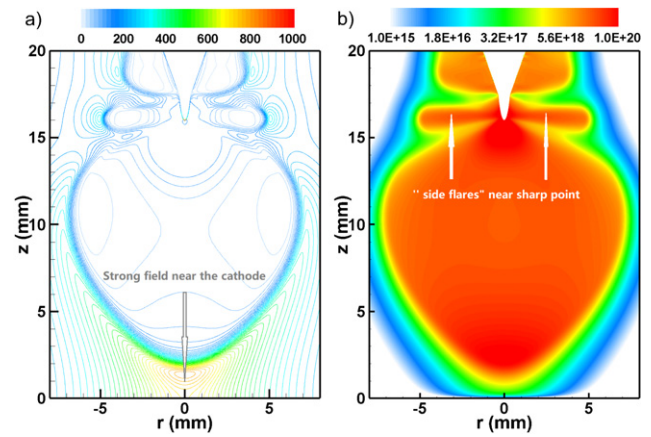


Figure 1. Test calculation of an overvoltage discharge in point-to-plane configuration. (a) The strong electric field near the cathode when the ionization head touching the end and (b) the side flares near the point electrode with $50 \mu\text{m}$ curvature radius of the pin. (The mesh distribution for this example is not presented in this paper).

However, the approach in paper [28] might not be able to be implemented directly to the point-to-plane configuration and even not always work for points with small curvature radius. The main reasons can be explained by a test calculation shown in figure 1. We tried to reproduce an 85 kV overvoltage discharge in a point-to-plane configuration with a pin of $50 \mu\text{m}$ curvature radius and 1.6 cm inter-electrode gap (the measurement can be found in [39, 40]) corresponding modeling work can be found in [41, 42] but the spark stage is not calculated. This experiment was recently conducted again in an E-FISH experiment [43], and similar experiments can be found in [40]. One of the main characteristics of this discharge is a large conical streamer structure. Difficulties arise when dealing with the time moment of the streamer touching the cathode plane: (i) For a point-to-point configuration, the strong electric field in the ionization heads disappear when streamers merge, the residual electric field is quite small and uniform in the channel; for a point-to-plane configuration, on the contrary, the electric field in the ionization head will be strengthened near the cathode, as shown in figure 1(a). There is always a very strong field in the cathode. If we freeze the field and increase it linearly with voltage, there will be non-physical large electric field near the cathode. (ii) For a point with small curvature radius and cross section radius, there will be side flares [40] generated on the surface of the point, as shown in figure 1(b). In this case, if the electric field is ‘frozen’ and increased linearly, there will be non-physical local ionizations near the point.

After the close of the plasma channel, the charge separation in the high density n_e and n_+ leads to considerable space charge, the generated polarization field impedes further violation of charge neutrality. Charge separation and the field adjust to each other so that the field restrains the runaway electrons and pulls forward the heavy ions, making them diffuse only a team. This diffusion is known as ambipolar [44]; another concept contrary to the ambipolar diffusion is free diffusion. The differences between such two concepts can be found in [44]. Literature [44] gives a standard to judge whether the species

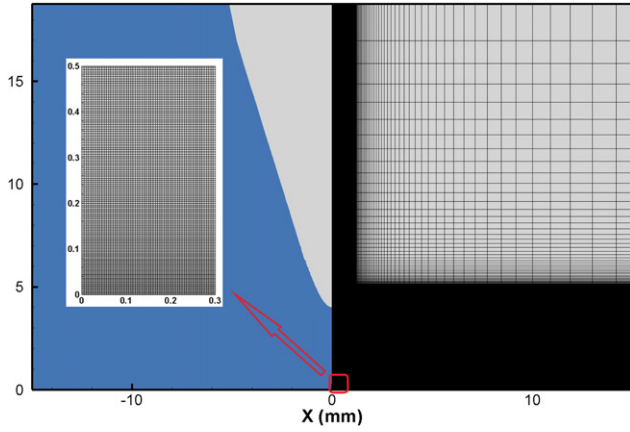


Figure 2. The geometry, computational domain and mesh distribution.

particles are undergoing ambipolar diffusion or free diffusion.

$$\frac{\delta n}{n} \approx \frac{\varepsilon_0 k T_e}{e^2 n} \frac{1}{R^2} = \left(\frac{d}{R}\right)^2, \quad d = \left(\frac{\varepsilon_0 k T_e}{e^2 n}\right)^{1/2} \quad (7)$$

where the quantity d is the Debye radius of the plasma, gives the distance characterizing strong charge separation and plasma polarization, and R is the length characterizing the scale of the charge density gradient. This is the distance over which the electron density varies considerably. If $R \gg d$ that is, if large density differences appear over distances greater than the Debye radius, then $\delta n/n \ll 1$, deviations from charge neutrality are small, and the diffusion is ambipolar. Take a typical condition in our paper as an example, for $T_e = 1 \sim 3$ eV, $n_e = 10^{19} \sim 10^{22} \text{ m}^{-3}$, and R is the radius of the plasma conductive channel, $R = 0.04$ cm, we have $d = 10^{-8} \sim 10^{-6}$ m, and $\delta n/n = 10^{-8} \sim 10^{-4}$, that is to say, the diffusion is clearly ambipolar.

Therefore, we introduce an ambipolar and Laplacian equation to model the spark in this work. This approach has been successfully used in the simulation of gliding arc discharges [45–47]. Assuming the drift-diffusion approximation, the species transport equation is as follows:

$$\frac{\partial n_i}{\partial t} + \nabla \cdot \Gamma_i = S_i \quad (8)$$

Differing from the original expression of the convection flux, the flux Γ_i of the ambipolar diffusion is written as follows:

$$\Gamma_i = -D_i \nabla n_i - (q_i/|q_i|) \mu_i n_i \mathbf{E}_{\text{ambi}} \quad (9)$$

The ambipolar electric field \mathbf{E}_{ambi} is derived from the plasma quasi-neutrality assumption, and the constraint can be written as in [48].

$$\sum_{i=1}^{N_{\text{ch}}} q_i \Gamma_i = 0, \quad \Gamma_e + \Gamma_n = \Gamma_p \quad (10)$$

where Γ_e , Γ_n and Γ_p represent flux for electrons, negative ions and positive ions, respectively. Combining equations (9) and

(10), we can get the expression of \mathbf{E}_{ambi} :

$$\mathbf{E}_{\text{ambi}} = \frac{\sum_i (q_i/|q_i|) D_i \nabla n_i}{\sum_i \mu_i n_i} \quad (11)$$

All notations in above equations have been explained in detail in section 2.1.

The electric field is obtained from the current conservation equation:

$$\nabla \cdot (-\sigma \nabla \Phi) = 0 \quad (12)$$

where the electric conductivity σ is defined as:

$$\sigma = e \sum_{i=1}^{N_{\text{ch}}} \mu_i n_i \quad (13)$$

The electric field is $\mathbf{E} = -\nabla \Phi$; note that this electric field is used for the calculation of the kinetics and electron transport parameters and it does not contribute directly to the convection flux in equation (9).

In fact, equation (12) can be derived from the charge conservation equation:

$$\frac{\partial \rho_c}{\partial t} + \nabla \cdot \mathbf{j}_c = 0 \quad (14)$$

where ρ_c is the net space charge density and $\mathbf{j}_c = \sigma \mathbf{E}$ is the current density, due to the quasi-neutrality assumption, equation (12) is equivalent to equation (14).

The use of the ambipolar equations and Laplacian equation is based on such a fact: the electron density gradient is much lower along the plasma conductive channel, and the timescale of chemical reactions significantly increases by about two orders of magnitude to $10^{-9} \sim 10^{-11}$ s compared with that of the discharge front in the streamer phase; this results in tiny charge separation and makes the ambipolar diffusion assumption reasonable. In this work the module for spark modeling is turned on if the dielectric relaxation time $\delta t_D < 10^{-15}$ s or the maximum electron density exceeds 10^{22} m^{-3} .

2.3. Global model for kinetics modeling

The contribution of kinetics to the streamer-to-spark transition during a post discharge stage between pulses (an order of ms magnitude). In such a long timescale, the 2D simulation is too time-consuming and computationally cost, and we may lose important information using the reduced kinetics scheme. Thus a global model is used assuming that, once the plasma channel forms after the ionization head, the average value of the species in the cross-sections of the quasi-neutral plasma region is adequately described by the 0D model.

ZDPlasKin code [33] with an incorporated BOLSIG + package [49] is used in this work. A system of ordinary differential equations for time-dependent densities of involved species during the period from 0 to 0.1 ms are solved. In section 4.3, the discharges for two different gas temperatures 300 and 600 K are discussed.

The kinetics scheme composed in paper [50] for $\text{N}_2 : \text{O}_2$ mixtures is used in this work. The scheme is based on the work of Pancheshnyi [51] and air kinetics developed by Kossyi

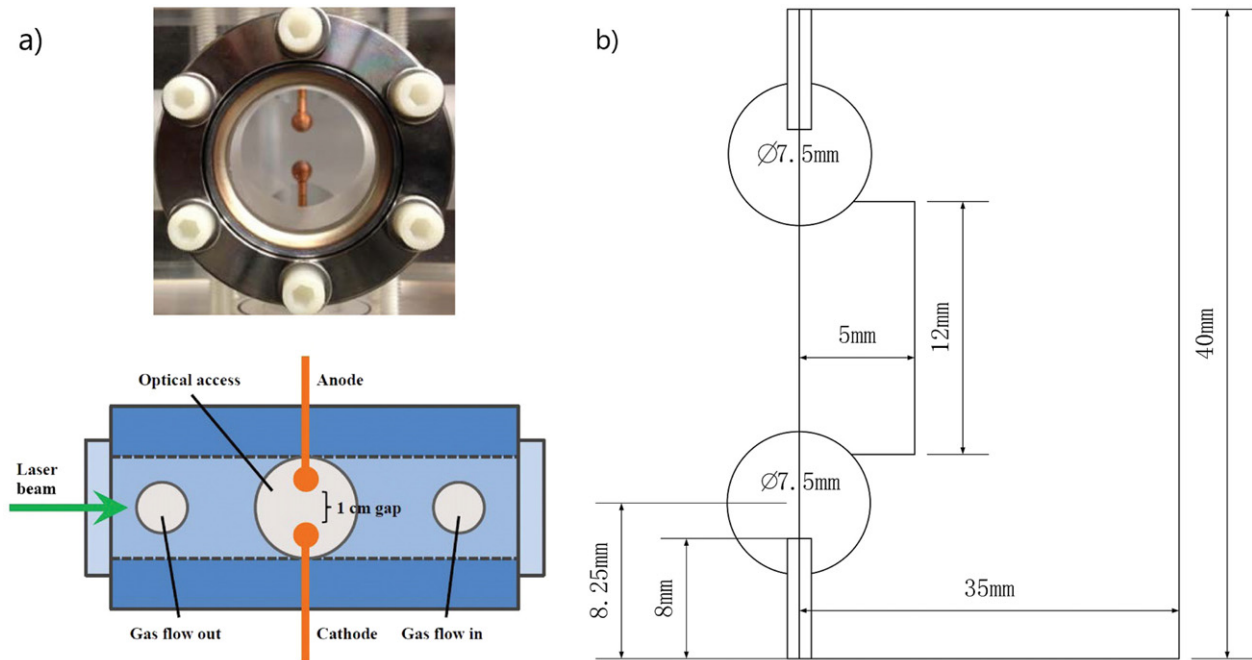


Figure 3. (a) Photograph and schematic of the discharge cell. The figure is extracted from [60]; (b) the geometry and computational domain for validation.

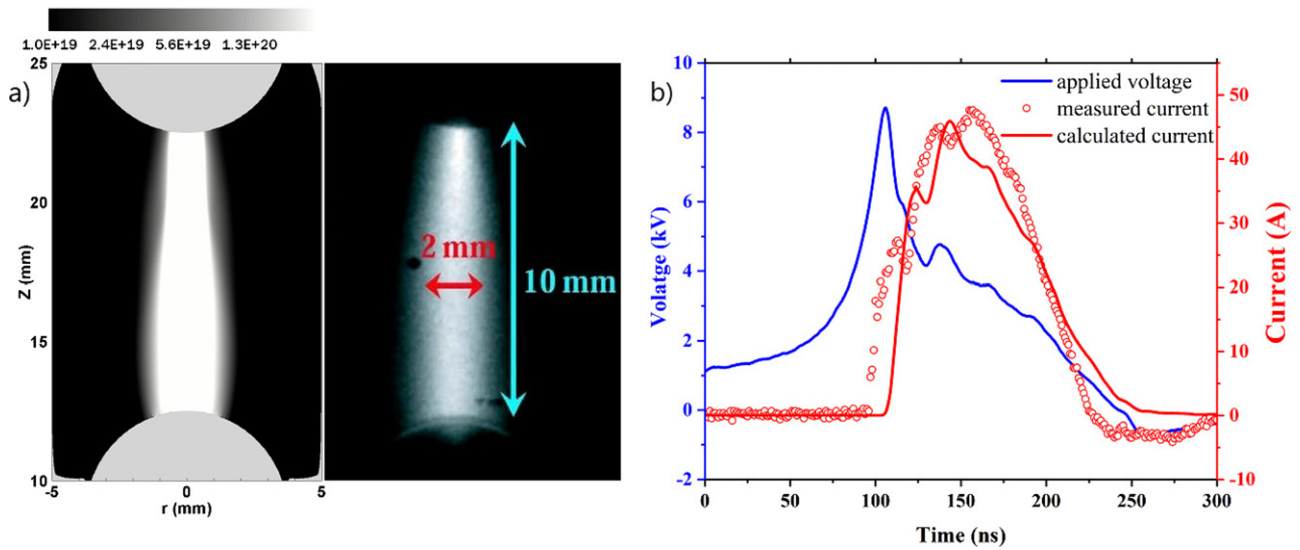


Figure 4. Validation with the point-to-point discharge experiment. (a) Comparison of the calculated $N_2(C^3\Pi_u)$ density during the pulse at 125 ns with ICCD camera images [57], (b) comparison of measured and calculated discharge current [60].

et al [52] and Cappitelli *et al* [53]. This scheme is originally composed to study the evolution of O-atoms in high specific deposited energy (0.1 eV mol^{-1}) and has been validated by optical emission spectroscopy experiments.

The kinetics scheme contains about 700 reactions, The following neutral, charged, excited molecules and atoms were taken into account: N_2 , $N_2(v = 1-8)$, $N_2(A^3\Sigma_u^+)$, $N_2(B^3\Pi_g)$, $N_2(a^1\Sigma_u^-)$, $N_2(C^3\Pi_u)$, N , $N(^2D)$, $N(^2P)$, N^+ , N_2^+ , N_3^+ , N_4^+ , O_2 , $O_2(v = 1-4)$, $O_2(a^1\Delta_g)$, $O_2(b^1\Sigma_g^+)$, $O_2(A^3\Sigma_u^+)$, $O_2(C^3\Delta_u)$, $O_2(c^1\Sigma_u^-)$, O , $O(^1D)$, $O(^1S)$, O_3 , O^+ , O_2^+ , O_4^+ , O^- , O_2^- , O_3^- , O_4^- , NO , NO^+ , NO^- , $O_2^+N_2$, N_2O , NO_2 , NO_3 , N_2O_5 , N_2O^+ ,

NO_2^+ , N_2O^- , NO_2^- , NO_3^- , e . In total, the scheme considered 55 species, including vibrational states of N_2 and O_2 .

A user-defined sensitivity module is coupled to the global model. By varying the rate of each reaction sequentially by 50%, the sensitivity coefficient $\varphi(t)_{i,r}$ is obtained by:

$$\varphi(t)_{i,r} = \frac{c(t)_{i,r=1.5r} - c(t)_{i,r}}{c(t)_{i,r}} \quad (15)$$

where r is a reaction rate for the i th reaction, and $c(t)_{i,r=1.5r}$ and $c(t)_{i,r}$ are the electron density under study with modified and non-modified rates, respectively. The threshold of ‘important’

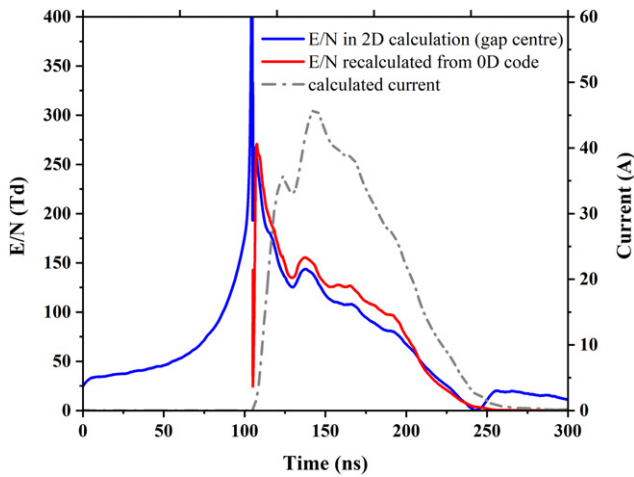


Figure 5. Comparison of the reduced electric field E/N at gap middle position in the spark from 2D code and 0D code.

reactions was set by the condition

$$\varphi(t)_{i,r} \gg 0.1 \quad (16)$$

for any time instant t . The sensitivity coefficients $\varphi(t)$ of the electron density for all reactions are obtained according to formula (15). For each reaction, the peak value of the sensitivity coefficient $\varphi(t)_{\max}$ corresponds to the maximum deviation from the initial unchanged density calculated with the kinetics scheme. The $\langle \varphi \rangle$ value averaged through the period of calculations is also calculated. This approach has been successfully used in an analysis of an actinometry experiment [50].

We use the kinetics model to probe a fixed point of the channel. The electric field and the initial electron density are extracted directly from the 2D calculation. The initial time instant of the 0D model is decided by the moment when the ionization front passed the fixed point of the discharge gap, in order to avoid the strong convection effect that offends against the homogeneous hypothesis of a 0D model. The electron density at the selected time instant from 2D calculation is used as the initial electron density. The electric field in time beyond the range of 2D model result is assumed as a Laplacian field that is much lower than the ionization threshold.

2.4. Geometries, initial and boundary conditions

The studied geometry is a point-to-plane electrode configuration with a 4 mm inter-electrode gap. As shown in figure 2, a stump hyperboloid shape with 300 μm of curvature radius is used to represent the point electrode: $(z/4)^2 - (r/1.1)^2 = 1$ (in unit mm).

A computational domain with 5 cm \times 5 cm in size in a cylindrical geometry is used. The mesh is refined to the size of 5 μm within 0.1 cm \times 0.5 cm domain, and is further refined to 2 μm near the cathode plane. In the rest of the computational domain the mesh size grows exponentially until the boundaries of the computational domain is reached. Note that the mesh implementation we mentioned above is just for the conditions with the gas temperature of 300 K at atmospheric pressure.

The initial electron density is assumed to be $n_{e0} = 10^{15} \text{ m}^{-3}$ uniformly distributed in the plasma domain to account for the residual electron density from prior pulses that occurs in the experiment. To ignite the discharge, a plasma spot with Gaussian distribution is distributed at the tip of the point electrode ($r = 0 \text{ mm}, z = 4 \text{ mm}$) by (in unit of m^{-3} and mm for number density and position, respectively)

$$n_e(r, z) = 10^{18} \exp\left(-\left(r/0.1\right)^2 - \left((z-4)/0.25\right)^2\right) \quad (17)$$

Initial ion density is given based on quasi-neutrality. The initial electron density is distributed according to the electric field near the point tip obtained by a one-step calculation of Poisson's equation.

The boundary conditions of the Poisson equation and Helmholtz equations are the same as described in paper [29, 30]. In this work, the waveform of the applied voltage to the point electrode is written as follows (in unit ns for time instant t and kV for applied voltage $U(t)$):

$$U(t)(\text{kV}) = \begin{cases} 7 & t \leq 10 \text{ ns} \\ 8.13 / (1 + \exp(0.1(t - 50))) - 1 & t > 10 \text{ ns} \end{cases} \quad (18)$$

The expression (18) is a fitting function of the waveform of the applied voltage from [26]. The voltage keeps 7 kV in time range 0 \sim 10 ns, and drops like a parabola in subsequent times. The value of the fitting formula in time range 0 \sim 60 ns is used as the input to 2D code PASSKEY.

For drift-diffusion equations, on the point electrode, the positive ion fluxes are set as zero while the negative species fluxes are estimated using the homogeneous Neumann conditions; on the cathode plane, the homogeneous Neumann condition $\nabla \cdot \mathbf{j}_c = 0$ is applied for all positive and negative charged species fluxes. It has to be noted that physically, the cathode flux is due to secondary electron emission. The reason of using this boundary condition has been discussed in paper [54]: in the framework of the fluid description, the boundary conditions at the cathode must be chosen in order to absorb the high space charge transported by the primary streamer head, otherwise the solutions would diverge even if secondary emission and photo-emission are taken into account. In fact, the homogeneous Neumann condition is derived from equation (14), a conductive current description $\nabla \cdot \mathbf{j}_c = 0$ takes places as soon as the streamer arrives at the cathode. Therefore, the homogeneous Neumann condition applied for all charged particle fluxes on the cathode can be regarded as an equivalent description of conductive current condition that facilitates and ensures the transition from a current wave propagation to a current conduction channel [54]. The radial flux of all charged species on the axis is set to zero.

3. Code validation

Two benchmarks of a volumetric streamer [32] and a surface streamer [55, 56] were reproduced by PASSKEY code as validations in the previous work [29]. In this work we present two direct validations with experimental results related with

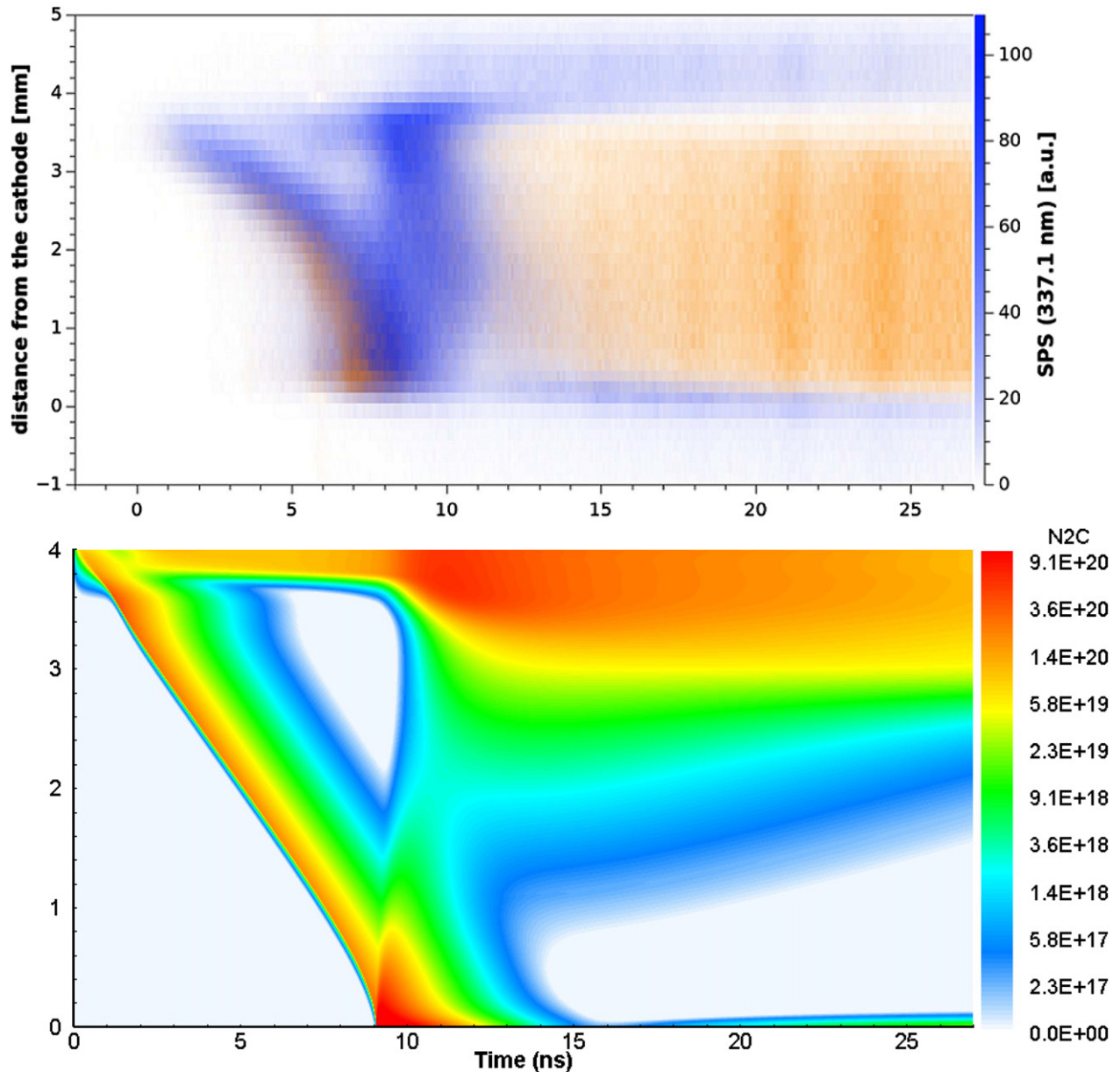


Figure 6. Comparison of the evolution of measured $N_2(C^3\Pi_u) \rightarrow N_2(B^3\Pi_g)$ emission intensity [26] and the calculated $N_2(C^3\Pi_u)$ density in a point-to-plane configuration.

streamer-to-spark transition: one in a point-to-point geometry [57–60] and another in a point-to-plane geometry [26].

3.1. Case 1: a point-to-point discharge

A comprehensive set of experimental and numerical data of the discharge morphology and dynamics, kinetics process and energy balance in nanosecond pulse discharges in air can be found in [57–60]. Most experiments for such studies were performed in a point-to-point discharge geometry discharge cell with two bare spherical electrodes. A rendering of the point-to-point geometry discharge cell is shown in figure 3(a), the discharge cell utilized bare spherical electrodes 7.5 mm in diameter, made of copper. The electrode gap was 1 cm. The anode was powered using a nanosecond pulsed generator pro-

ducing 10 kV peak voltage pulses ~ 100 ns duration, at the pulse repetition rates of up to $f = 10$ kHz, while the cathode was grounded. The point-to-point discharge was operated in air at ambient temperature and 100 Torr pressure.

The computational domain and geometry set in the code is presented in figure 3(b). The waveform of the applied voltage powering in the anode is shown in figure 4(b). The distribution of the $N_2(C^3\Pi_u)$ density and the electrical current is calculated and shown in figure 4(a), together with measured results in paper [57, 60]. The calculate spark morphology agrees well with the measurements in channel width and emission distribution, the calculated current also fits that in the experiment.

To check whether the global model can be used for the spark phase and to validate the kinetics, we did a cross check

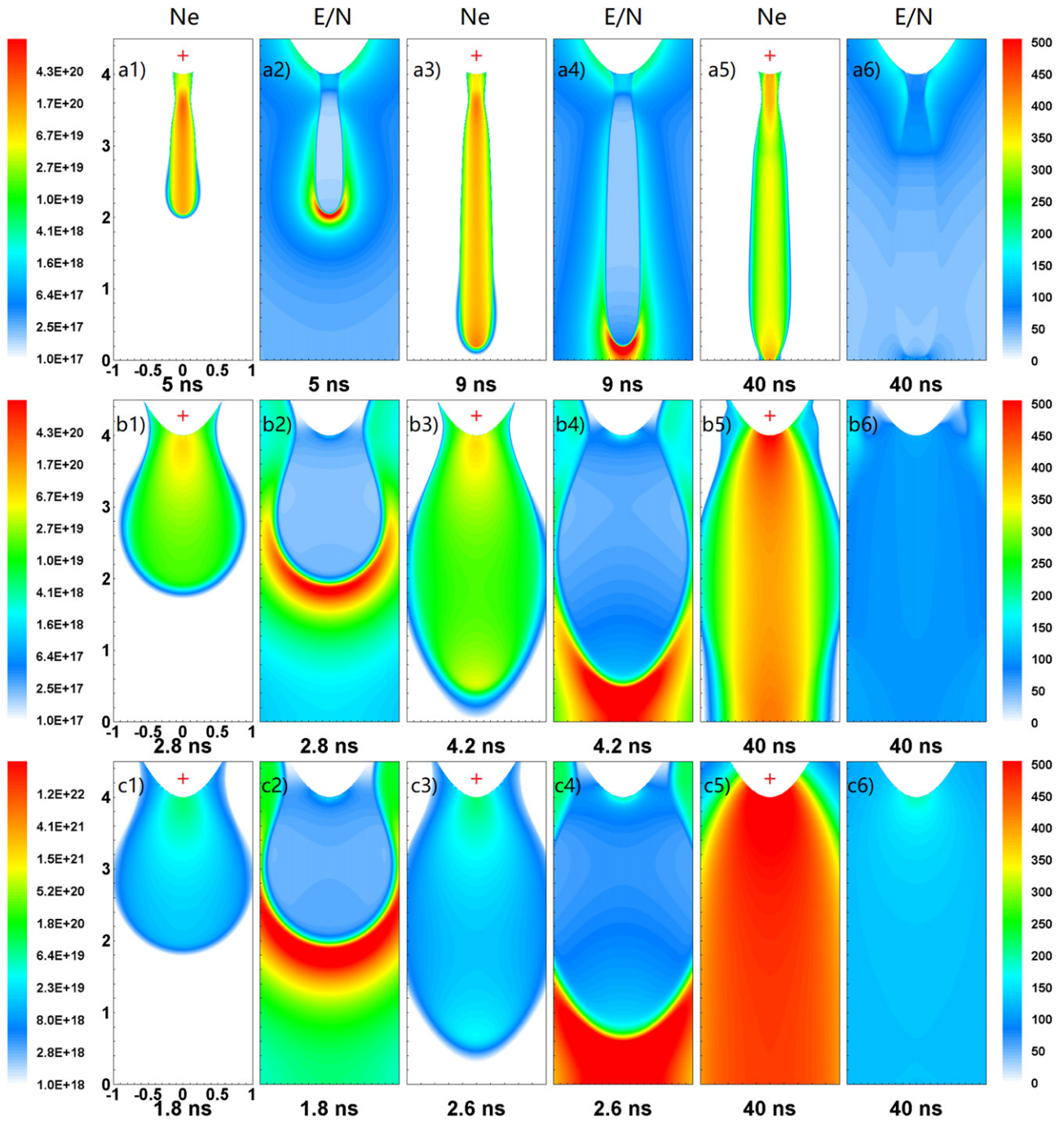


Figure 7. The calculated electron density and the electric field at 300 (a1 ~ a6), 600 (b1 ~ b6) and 800 K (c1 ~ c6). The unit of the scale on both the x or y direction is mm.

by running the 0D code and current value extracted from 2D modeling in figure 4(b) to recalculate the electric field after the ionization front. The initial electron density is the electron density at $z = 18$ mm from 2D calculation, the value is 10^{13} cm^{-3} . The electric field E/N is derived by $E(t) = I(t)/(q\mu_n(t)\pi r^2)$, where t is the time instant after the formation of the channel, $I(t)$ and $E(t)$ are the current and the electric field at the t moment, respectively, q is the unit charge, $\mu(E/N)$ is the electron mobility calculated from the Boltzmann solver [49], and r is the radius of the channel (2 mm in this work). The recalculated electric field and the field calculated by 2D modeling

are shown together in figure 5, after some iterations of electric field at beginning, the 0D code produced a series of E/N similar in value and trends with that of 2D results, indicating that both 2D and 0D modeling can be used to study the spark phase.

3.2. Case 2: a point-to-plane discharge

There are very few streamer-spark experiments with a data set as complete as case 1. A compromise benchmark experiment [26] conducted at atmospheric pressure is chosen. The geometry of the discharge configuration, the initial and boundary

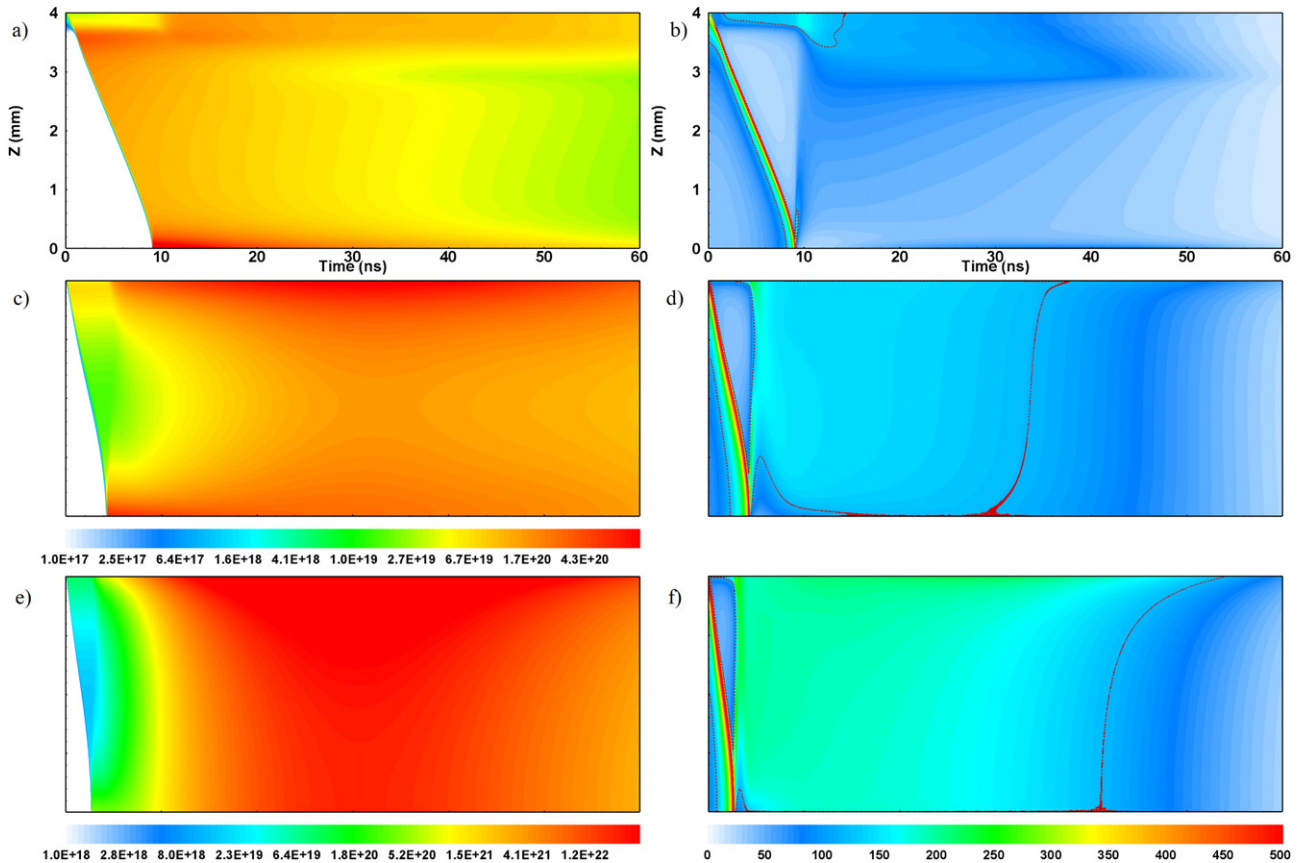


Figure 8. The time evolution of the electron density and the electric field along the streamer propagation axis $r = 0$ for the discharges at (a) and (b) 300, (c) and (d) 600, (e) and (f) 800 K. These six sub-figures use the same legends as figure 7. The red dashed line in figures 8(b), (d) and (f) is 120 Td contour line—ionization threshold of air, is plotted as a reference.

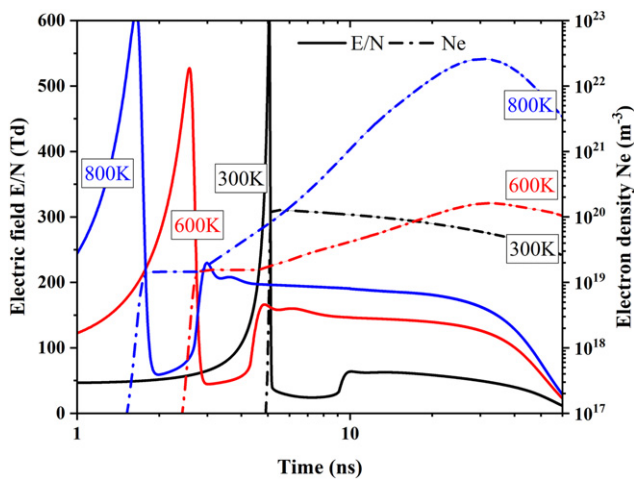


Figure 9. The time evolution of the electron density and electric field at the middle of the gap ($r = 0$, $z = 2$ mm) at 300, 600 and 800 K in the first 60 ns.

conditions of the problem have been described in section 2.4 in detail.

Figure 6 shows the evolution of the calculated axial $N_2(C^3\Pi_u)$ density versus time and the cross-correlation spectroscopy record of the $N_2(C^3\Pi_u) \rightarrow N_2(B^3\Pi_g)$ (the second positive system) emission intensity, the morphology qualitatively agrees with the experimental results. A positive streamer

starts in the tip of the anode and reaches the cathode at about 9 ns, the formation of a secondary streamer in the proximity of the anode is captured both in experiment and in simulation. The $N_2(C^3\Pi_u)$ density decays after the channel is closed as a result of the decreasing electric field.

4. Results and discussions

4.1. Discharge evolution at different temperatures

In this section, the evolution of streamers and sparks in air uniformly preheated to 300, 600 and 800 K are presented.

The electron density and the electric field distribution at time moments of streamer propagation, approaching cathode and gap bridging in 300, 600, 800 K are shown in figure 7. The average velocities for three streamers varies between $4 \times 10^5 \sim 2 \times 10^6$ m s⁻¹, which are in agreement with previous studies [61, 62]. For all cases, the streamers form near the anode, expand during propagation and finally penetrate the gap. When the streamers are approaching the cathode, the electric fields are significantly strengthened between the ionization fronts and the cathode (figures 7(a4)–(b4)). When gas temperature is 300 K, the positive streamer touches the end at about 9 ns (figure 7(a3)), the field near the cathode is up to 600 Td (figure 7(a4)), the average propagation velocity is

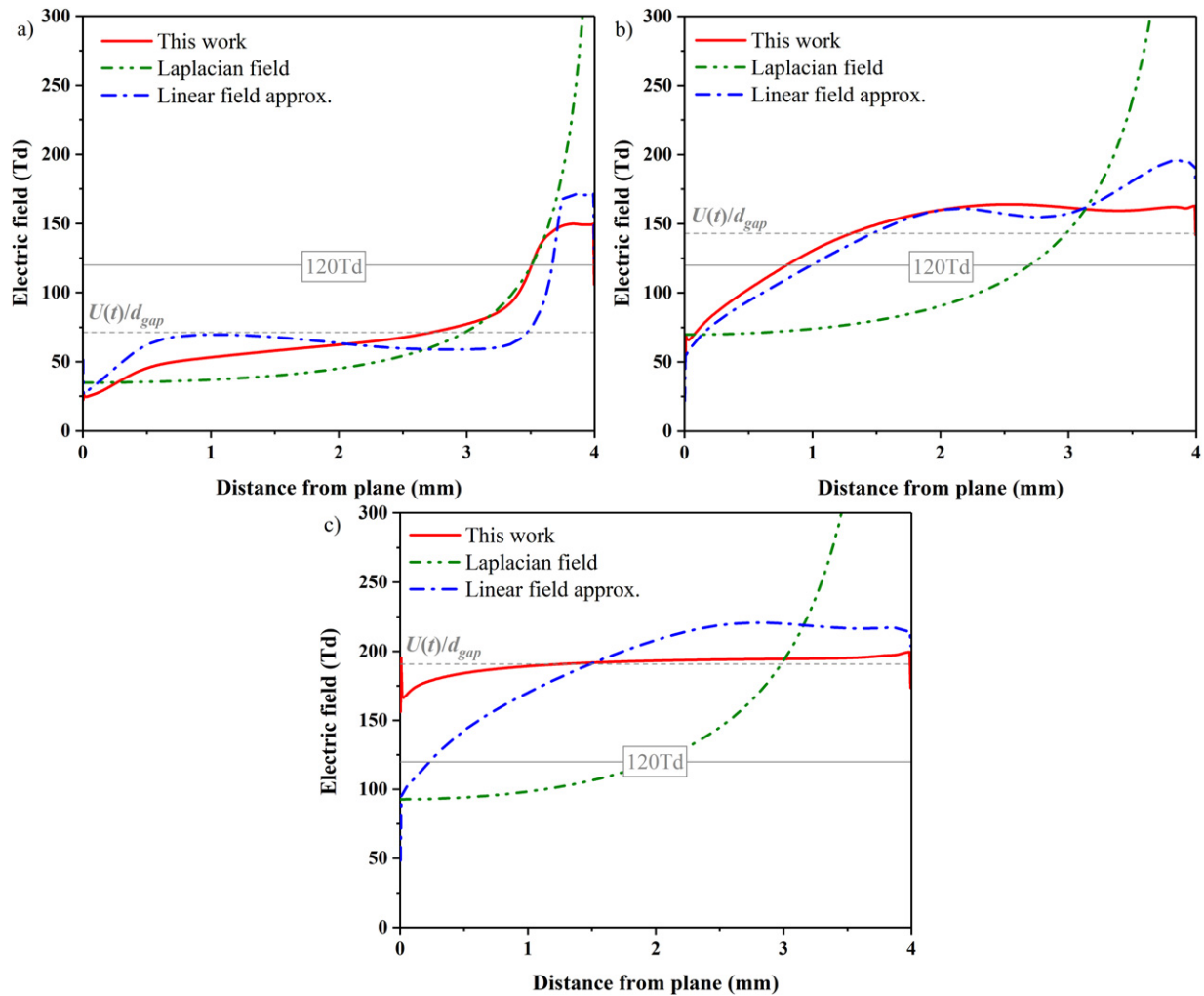


Figure 10. The axial distribution of reduced electric field calculated in this work and by linear field approximation at 14 ($U = 6.91$ kV), 9.2 ($U = 7$ kV) and 7.6 ns ($U = 7$ kV) for 300, 600 and 800 K cases, respectively. Linear field approximation means the electric field varying proportional to applied voltage after gap closing at 10 ns ($U = 7$ kV) for (a) 300 K case, 5.2 ns ($U = 7$ kV) for (b) 600 K case and 3.6 ns ($U = 7$ kV) for (c) 800 K. The average field $U(t)/d_{gap}$, the ionization threshold field (120 Td for air) and the Laplacian field are also plotted for each case as references.

1.4×10^5 m s $^{-1}$. The streamer shows a narrow channel with a nearly constant 200 μ m curvature radius ionization front during the whole streamer propagation stage, the higher electron density accumulation in the close vicinity of the streamer propagation axis $r = 0$ can be observed, the similar result was also obtained in a simulation for a point-to-plane positive corona discharge [54].

As the gas is preheated to higher temperatures 600 K or 800 K, the gas density decreases accordingly, leading to higher reduced electric field in the entire region, and the discharges turn to be more diffusive. Figures 7(b1)–(b4) and (c1)–(c4) shows that, in the 600 and 800 K cases, the radii of ionization fronts grow to the maximum when reaching the middle of gap. The average propagation velocity increases to 9.5×10^5 m s $^{-1}$ and 15×10^5 m s $^{-1}$, respectively.

Once the streamer reaches the end, the electron density increases dramatically at higher temperatures 600 K and 800 K, large conductive channels with radii 500–1000 μ m are formed as is shown in figures 7(b5) and (c5). At 600 K and

800 K, the electric field is also higher comparing with that of the 300 K case.

The full maps of time evolution of the axial electron density and electric field are shown in figure 8. The so-called ‘secondary streamer’ [17] with electron density increase and electric field enhancement near the anode are observed for all cases right after the gap is closed, the maximum electron density is observed near the electrodes. In the 300 K case (figures 8(a) and (b)), both electron density and electric field in the whole channel decrease after the secondary streamer. But for elevated temperatures 600 and 800 K (figures 8(c) ~ (f)), the field decreases but electron density first increases to a higher value and then decreases.

The differences of electron and field evolution for 3 cases is related directly to the ionization threshold of studied gas (120 Td for air in this work). The 120 Td contour lines are drawn in figures 8(b), (d) and (f) as a reference to indicate the boundary of electron density increase/decrease region. A deeper insight can be achieved by plotting the time evolution

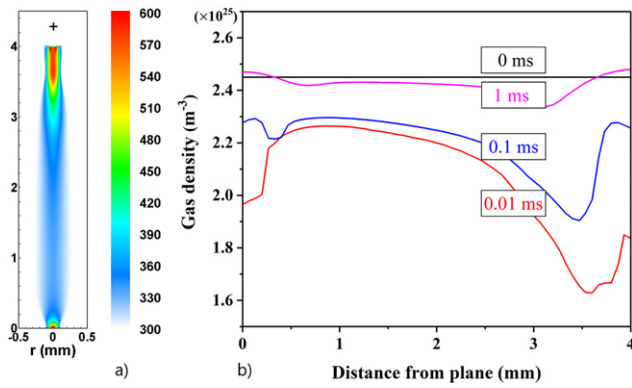


Figure 11. (a) The temperature distribution at the end of first pulse for the discharge at 300 K; (b) the axial gas density distribution caused by the first pulse at different time moments 0.01, 0.1 and 1 ms. Figure 11(a) and ‘0 ms’ line in figure 11(b) is obtained by fully coupling equations mentioned in section 2.1, ‘0.01 ms’, ‘0.1 ms’ and ‘1 ms’ lines in figure 11(b) are obtained just by solving Euler equations.

of electron density and reduced electric field in the gap middle ($r = 0$, $z = 2$ mm), as shown in figure 9. At 300 K, the electron density rapidly increases by three orders of magnitude and reaches up to 10^{20} m^{-3} after the ionization front, then decays immediately in the low field below 70 Td. At 600 and 800 K, the electron density reaches $2 \times 10^{19} \text{ m}^{-3}$ due to the ionization fronts, an order of magnitude lower than that in 300 K case. The electric field of 600 and 800 K cases rapidly decreases from 600 Td to below 70 Td before the gap closing, the electron density keeps approximately constant in this stage. After the channels’ formation, the electric field rapidly increases to 165 Td for 600 K case and 226 Td for 800 K case, the electron density increases by one orders of magnitude to $1.6 \times 10^{20} \text{ m}^{-3}$ at 600 K, and by two orders of magnitude to $2.6 \times 10^{22} \text{ m}^{-3}$ at 800 K. Then the electron density for 600 and 800 K cases decreases due to the decreasing electric field.

In reference [27], a rough criteria of streamer-to-spark transition for point-to-point configuration discharge has been mentioned (we name it ‘criteria 1’ in the following text): if the electric field in the channel is higher than the breakdown field, the streamer-to-spark transition may occur in the whole channel. The electric field can be estimated by U/d_{gap} due to the uniformity. The ‘criteria 1’ can be expressed as

$$T \geq \frac{(E/N)_{\text{threshold}} P d_{\text{gap}}}{k_b U} \quad (19)$$

where k_b is the Boltzmann constant, d_{gap} is the length of inter-electrode gap (4 mm in this work), $(E/N)_{\text{threshold}}$ is 120 Td for air.

The electric field in a point-to-plane geometry differs because near the cathode, the electric field is relatively lower due to the electric field reflection (return strokes). Whether or not the estimation criteria is suitable for the point-to-plane configuration are discussed in the following sections.

4.2. Streamer-to-spark transition in the first pulse

We consider that a spark is formed if the entire axial electron density increases by at least one order of magnitude after the

formation of the conductive channel. According to figure 8, only the 800 K case meets this condition, while the 600 K case is on the critical point of transition. To understand the underlying reasons, we plot the calculated axial electric field, Laplacian field, the field based on linear approximation, the average field and the ionization threshold electric field together for 300 K, 600 K and 800 K cases in figure 10. The time moments are 5 ns after the formation of the channels, these time moments correspond to the finish of the secondary streamer.

The field in figure 10 differs significantly from each other. The electric field based on linear approximation is rather non-uniform and decreases toward the cathode, because the linear field approximation ‘freezes’ the electric field during the secondary streamer formation, and thus cannot represent the field in the subsequent conduction stage. It can be found that, at higher temperature when the streamer is diffusive the calculated field and average field agree well in the main channel, but calculated field is lower near the cathode.

For the 300 K case, all the field is below the ionization threshold, there is no spark formation. For the 600 K case, the calculated and average electric field (145 Td) is slightly higher than the ionization threshold in the channel, while the linearly approximated field is below 120 Td near the cathode, the electron density increases slightly but does not exceeds one magnitude higher. At 800 K, the calculated and average electric field (190 Td) are significantly higher than the ionization threshold, and the electron density increases by two magnitudes of orders within 50 ns.

Above analysis is based on ‘criteria 1’, but it is not always ‘safe’ for the point-to-plane discharges (e.g. the 600 K case the spark is not formed). The main reason is that, when the streamer touches the cathode, there is a return stroke weakening the channel electric field near the cathode (this region can expand several mm) due to the electric conductivity mismatching in the formed channel. As a result, the field in the plasma channel is not always as uniform as that in a point-to-point discharge conditions. At such condition, the criteria 1 (based on the average electric field U/d_{gap}) might be used together with an additional ‘criteria 2’ based on the Laplacian field:

$$(E/N)_{\text{Laplacian}} \geq (E/N)_{\text{threshold}} \quad (20)$$

The Laplacian field near the cathode is always close to or lower than the results from 2D model (see figure 10), and can be easily obtained by existing commercial softwares or by a simple in-house code, thus is capable to be considered as a ‘more conservative’ criteria.

Equation (20) can be rewritten taken into consideration the ideal gas law and the existing analytical electric field solution of point-to-plane geometry [63, 64]:

$$|E(0,0)| = \frac{1}{\Xi(0,0)} \frac{A}{1 - \xi^2(0,0)} \geq E_{\text{threshold}} \quad (21)$$

where A is a constant depending on the electrical potential of the point electrode and its shape, A is written as follows:

$$A = \frac{2V_a}{\log\left(\frac{1+\xi_0}{1-\xi_0}\right)} \quad (22)$$

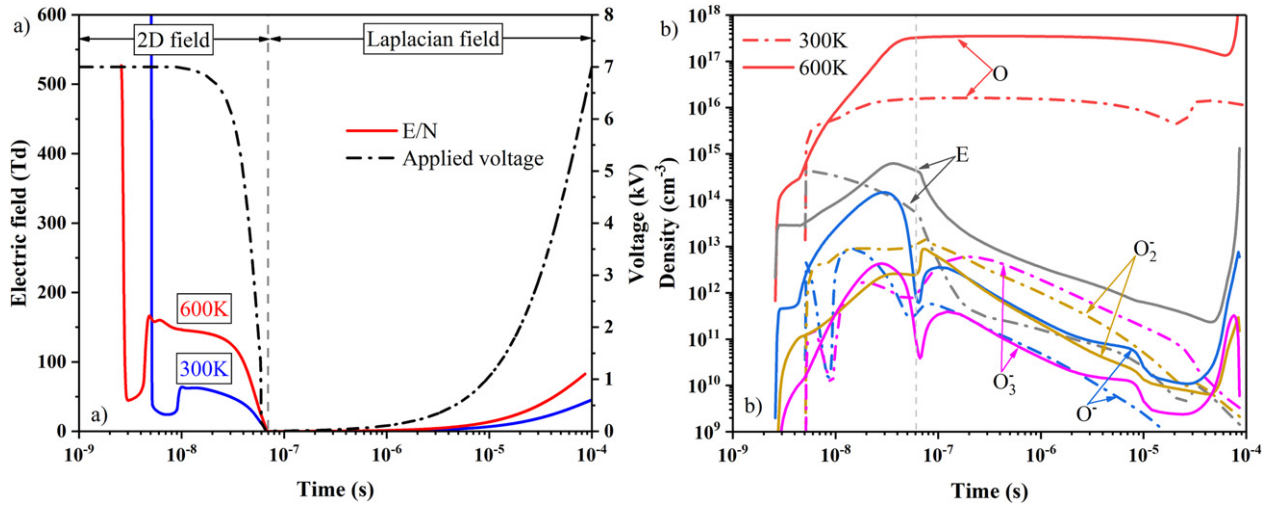


Figure 12. (a) The reduced electric field used for kinetics modeling at 300 and 600 K and the applied voltage. The reduced electric fields in time range 0 ~ 60 ns are extracted from the 2D results, in time range 60 ns ~ 0.1 ms we assume a Laplacian distribution throughout the channel; (b) the time evolution of electrons, O-atoms, O⁻, O₂, and O₃ at 300 and 600 K.

where V_a is the electrical potential of the point electrode. For the surface of a point electrode can be characterized as the hyperbola $z^2/a^2 - r^2/b^2 = 1$, ξ_0 in formula (22) is determined as $\xi_0 = a/\sqrt{a^2 + b^2}$, and $\Xi(0, 0) = \sqrt{a^2 + b^2}$. Combining equation (20) ~ (22), the ‘criteria 2’ can be expressed as

$$T \geq \frac{(E/N)_{\text{threshold}} P l_s}{k_b U} \quad (23)$$

where l_s is an ‘equivalent uniform channel length’ only depending on the shape of the point electrode,

$$l_s = \frac{\sqrt{a^2 + b^2}}{2} \log \left(\frac{\sqrt{a^2 + b^2} + a}{\sqrt{a^2 + b^2} - a} \right) \quad (24)$$

The estimated transition temperature of the studied geometry in this paper at given voltage, is 1046 K. This value agrees with the value proposed in references [22, 25], 1000 ± 125 K. As a conservative estimation, this value is higher than the numerically predicted 800 K.

The analysis above are all conducted assuming uniformly preheated gas. The streamer-to-spark transition may also occur in gases heated by previous discharges. In that case, the density distribution in the plasma channel is non-homogeneous. As a trial, we calculated the temperature distribution at the end of first pulse by fully coupling the equations mentioned in section 2.1, and plotted the axial gas density due to fluid expansion after the first pulse in figure 11 at different time moments. It is clearly seen that there are strong heating region near the electrodes, and the gas density is greatly reduced within 0.01 ms (corresponding to 100 kHz) to $1.6 \times 10^{25} \text{ m}^{-3}$. At high repetitive frequencies, the discharges can quickly transit into sparks due to the low gas density and increased E/N in the channel.

In this section we concluded that at 600 K, the streamer-to-spark transition does not occur in the first pulse for the geometry studied in this work. Previous research reported

that [22, 26], at 10 kHz and 500–600 K preheated air, the net electron production rate is always positive, but the mechanism is not clear. This fact means that sparks could still form in the post discharge stage at low temperatures and electric field due to the gas temperature increase or reactive species produced during the discharge stage. In the following section, the mechanism of spark formation at low temperatures and electric field is studied based on kinetics analysis.

4.3. Spark formation at post discharge stage

The evolution of species after the discharge gap closing is studied using a global model in this section. The studied temperature is 300 and 600 K, respectively, and the frequency is 10 kHz. We probe the evolution of species in the central point of inter-electrode gap ($r = 0$, $z = 2$ mm) till 0.1 ms after gap closing.

The reduced electric field as an input function for the global code, is decided according to different time moments. In the first 60 ns, after the ionization wave passed the probed point, the reduced electric field is extracted from the 2D results directly; after the first 60 ns, the field drops below 1 Td, the plasma density is still high but the charge separation is weak. We used only the Laplacian field calculated in the 2D code as the input. The applied voltage determining Laplacian field during post discharge stage is taken from the experimental waveforms [21, 22]:

$$U(t) = U_{00} \left[1 - \exp \left(-\frac{t}{RC} \right) \right] \quad (25)$$

where U_{00} , R and C represent the generator voltage ($O(10)$ kV), current limiting resistor ($O(1 \sim 10)$ M Ω) and total capacity ($O(10)$ pF) of the electric circuit, respectively. In this work, $U_{00} = 11.1$ kV, $RC = 10^{-4}$ s. Figure 12(a) shows the reduced electric field for the 300 and 600 K cases, as well as the applied voltage. The field during the secondary streamer stage

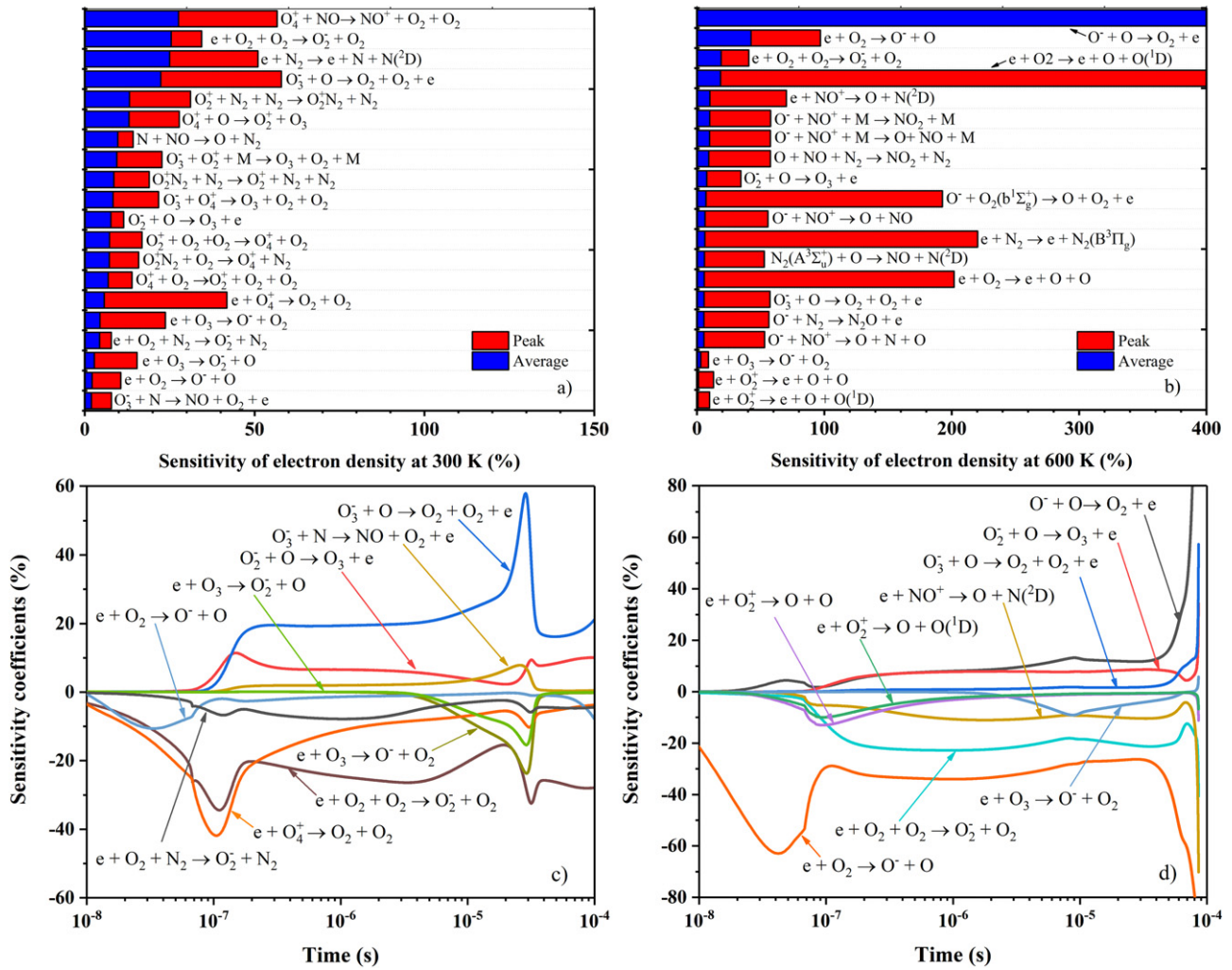


Figure 13. Absolute values of the peak and average sensitivity coefficients of top 20 reactions (selected by the average sensitivity coefficients) for (a) 300 K and (b) 600 K; the time evolution of sensitivity coefficients of selected reactions for (c) 300 and (d) 600 K case. The ionization reactions of N_2 and O_2 are not plotted in figures 13(a) and (c), and the ionization reactions of N_2 , O_2 and O-atom are not plotted in figures 13(b) and (d), because the ionization reactions during strong-field stage (when the discharge front reaches the fixed point, and the streamer-to-spark transition stage) are not our focus.

is below 70 Td in time range $10 \sim 60$ ns for 300 K case, while above 120 Td in time range $5 \sim 33$ ns for 600 K case. The maximum field at post discharge stage is 45 and 82 Td for 300 and 600 K cases, respectively. For both cases, the field at post discharge stage is much lower than the ionization threshold of air. The initial electron density for the global code is extracted from 2D results: $1.04 \times 10^{13} \text{ cm}^{-3}$ and $1.58 \times 10^{12} \text{ cm}^{-3}$ for 300 and 600 K case, respectively.

The time evolution of charged species of interest: electrons, O^- , O_2^- , O_3^- and O-atoms as products of dissociative attachment reactions are presented in figure 12(b). The density of the species increases sharply before 10 ns after the ionization fronts. At 60 ns the E/N input is switched from the consistent 2D results to the artificially given Laplacian field, the discontinuity of $E/N(t)$ leads to a sudden rise/drop of the density of O^- , O_2^- and O_3^- again. This sudden change is not strictly physical, but nevertheless provides the basic information required for the following post discharge stage for further analysis.

Significant differences between the two cases are shown in figure 12(b): (i) the electron, O^- and O-atom densities are significantly higher for 600 K than those of 300 K, while O_2^- and O_3^- density is lower than that of the 300 K case. (ii) The electron, O^- , O_2^- density increase dramatically at 600 K by 2–3 orders of magnitude at around 0.05 ms. The sharp increase of electron density indicates that the spark is initiated again in the channel at a much lower electric field and temperature (75 Td and 600 K). To understand how electron density are preserved after the pulse at 300 K and 600 K, and to explain for the sharp increase of electron density at the end of post discharge stage at 600 K, a sensitivity analysis is conducted.

Figures 13(a) and (c) show the key reactions that electrons are sensitive to, and the time evolution of the sensitivity coefficients at 300 K. The electron density is sensitive mainly to the electron detachment reaction from O_3^- due to collision with O-atoms and N-atoms, three-body attachment with O_2 , dissociative attachment reaction with O_3 and dissociative recombination with O_4^+ :

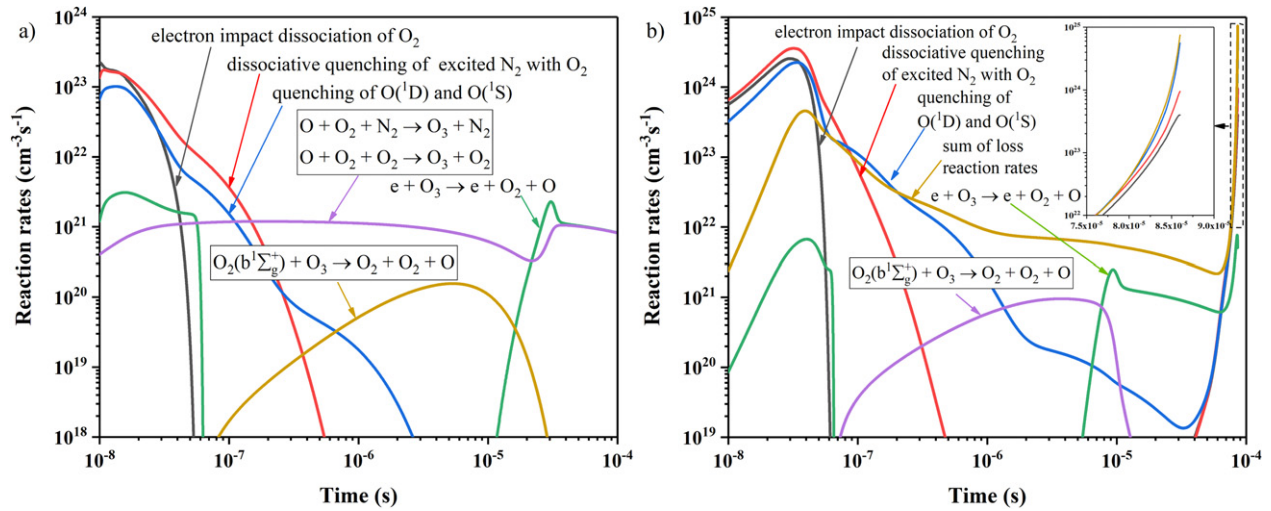
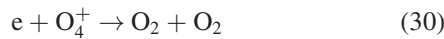
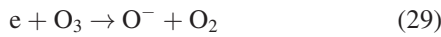
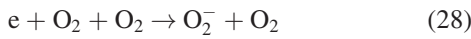
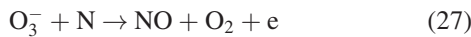
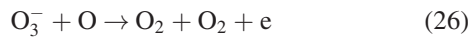
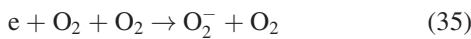
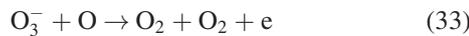
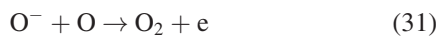


Figure 14. Rates of reactions responsible for production and loss of O-atoms at (a) 300 K and (b) 600 K. Three sets of reactions contributing to O-atoms production are combined for a clear vision.



Figures 13(b) and (d) show the key reactions responsible for the electron variations and the sensitivity coefficients of electron related reactions at 600 K. It is interesting to find that, the dominating processes for electron density variations during the post discharge stage are rather different with the 300 K case, electron detachment from O^- , O_2^- and O_3^- , dissociative attachment and three-body attachment reactions with O_2 are more sensitive:



For both cases, O-atoms and O_3^- are important reactants in reactions producing electrons. As the density of O-atoms is much higher than that of O_3^- , we can come to the conclusion that high density O atoms could ‘knock off’ electrons from negative charged species during the post discharge stage, they play a central role in maintaining electron density and initiating streamer-to-spark transition.

From the rate analysis of O-atoms presented in figure 14, we can find that for both cases, the O atoms are produced mainly by electron impact dissociation of O_2 during the pulse. After the pulse, the O atoms are sustained by quenching of excited

N_2 with O_2 before 1 μs , then by quenching of $\text{O}(^1\text{D})$ and $\text{O}(^1\text{S})$ with N_2 and dissociation of ozone in the following time. It has to be noted that, at the end of post discharge stage, the rate of dissociation of ozone by electron impact increases dramatically, the increase leads to a jump of O-atoms density at 0.03 ms for 300 K and to a drop of negative charged ions O^- and O_3^- , see figure 12(b).

Besides detachment reactions, electrons could also be generated through ionization from excited species, for example the associative ionization of $\text{N}_2(\text{A}^3\Sigma_u^+)$, stepwise ionization of $\text{O}_2(\text{a}^1\Delta_g)$ [26, 52] or other species with lower ionization threshold energy such as O-atoms. Those reactions occur only when the field increase and the excited species are dense in the last stage, the sensitivity analysis may not capture them. Therefore an additional rate analysis is conducted for electron related reactions, shown in figure 15.

At 300 K, the main reaction responsible for direct production of electrons is the electron detachment reaction of O_3^- while the loss is dominated by three-body attachment. The jump of reaction rates at 0.03 ms in figures 15(a) and (b) is due to the increase of O-atoms from electron impact ozone dissociation when the electric field reaches 15–20 Td.

At 600 K, the main electron related reactions correspond to equations (31)–(35) before 0.05 ms after pulse. There are slight drops of reaction rates related with O^- and O_3^- in figure 15(c); at that moment, the electric field reaches 10–15 Td, and the decrease of ozone density is accelerated because of electron impact ozone dissociation, shown in figure 14(b). After 0.05 ms in the 600 K case, the field increase to 50–75 Td, the rate of electron impact ionization, stepwise ionization and associative ionizations increase dramatically. It is clearly seen that, the influence of stepwise ionizations, associative ionizations become significant only when the electron density and excited species are high enough after 0.05 ms, they can accelerate the population of electron density when the spark is ignited, but the direct contribution of electron population still comes from electron detachment reactions of negative charged species O_3^- , O_2^- and O^- .

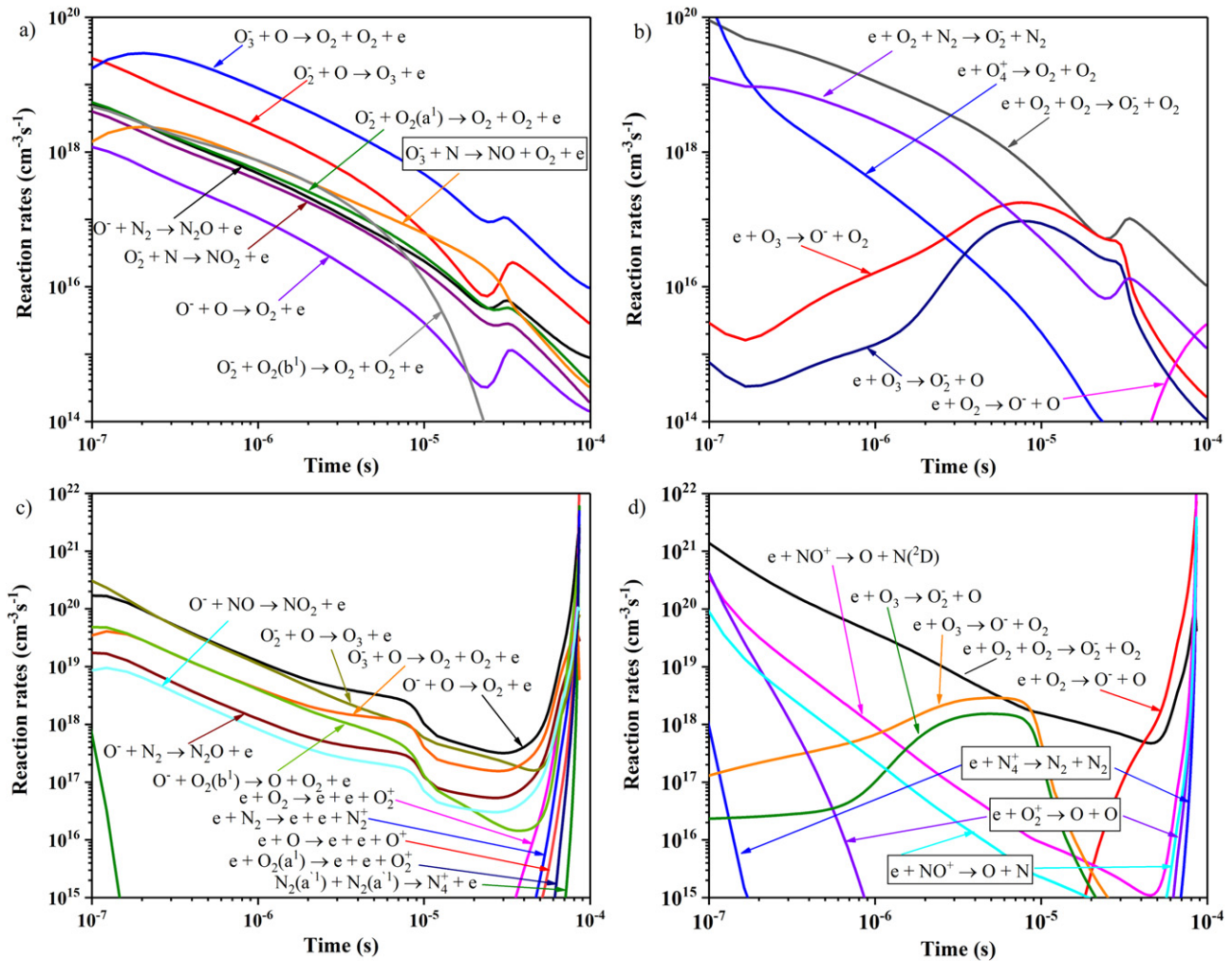


Figure 15. Rates of the main reactions responsible for (a) production and (b) loss of electrons at 300 K; rates of the main reactions responsible for (c) production and (d) loss of electrons at 600 K.

To summarize, the streamer-to-spark transition can happen in a lower than ionization threshold field and low temperature (600 K), if the following conditions are met: (i) a plasma channel is already formed during the previous pulses, thus a spark can be re-ignited in the residual plasma column over the entire gap. Otherwise there will be a streamer formation near the point again. (ii) High density of O-atoms is formed in the last pulse. The O-atoms play a vital role in knocking the electrons off the negative charged species. (iii) The reduced electric field reaches 50–75 Td, so that three-body attachment reactions are suppressed, the ozone (which also attaches electrons) is dissociated and electrons stored in negative charged species can be released through collision with O-atoms. The rate of associative ionizations and stepwise ionizations from excited species also increase dramatically at this field.

An example can be found in the early work by Naidis [19], where the streamer-to-spark transition is studied in a shorter timescale based on kinetics analysis. In the work of [19], the electric field after gap closing is 76–96 Td, and the accumulation of O-atoms finally lead to the formation of the spark, agreeing well with the aforementioned conditions required for spark formation at lower field and temperatures.

5. Conclusions

The streamer-to-spark transition in a point-to-plane configuration in atmospheric pressure air is studied by a 2D–0D combined approach. The PASSKEY code validated by experimental data in existing papers [26, 57, 60] and ZDPlasKin code with an user-defined sensitivity analysis module are used.

Evolution of discharge parameters at 300, 600 and 800 K are studied by 2D numerical calculation. Increase of gas temperature leads to higher propagation velocity and streamer radius. Higher electron density is achieved at 300 K during the streamer propagation stage but more electrons are produced during the secondary streamer and spark phase at 600 and 800 K. When the electric field is smaller than the ionization threshold field (120 Td) the electrons begin to decay.

In the first pulse, the streamer-to-spark transition occurs when temperature is higher than 800 K, the electron density in the whole gap increased by over one order of magnitude. A conservative criterion is proposed to decide the spark formation condition: the Laplacian field near the plane electrode should be higher than the ionization threshold. An analytical expression is given, and the predicted transition temperature

in the first pulse is 1046 K, agreeing with the experimental observation 1000 ± 125 K.

The influence of non-homogeneous temperature distribution on streamer-to-spark transition is qualitatively estimated. The fluid responses after the first pulse at 300 K is calculated. The gas density near two electrodes decreases by 36% to $1.6 \times 10^{25} \text{ m}^{-3}$ 0.01 ms after the pulse (corresponding to 100 kHz repetitive frequency) and by 20% to $1.9 \times 10^{25} \text{ m}^{-3}$ (corresponding to 10 kHz repetitive frequency) near the anode, indicating that the discharge could quickly transit into spark due to the increase of E/N .

0D kinetics modeling is used to study the streamer-to-spark transition during the post discharge stage with a long duration of 0.1 ms. Discharges at 300 and 600 K are studied and compared. The field as the input to global model is extracted from the 2D calculation. The electric field during post discharge stage for both cases is much lower than ionization threshold. The streamer-to-spark transition occurs at 600 K case. High density O-atoms play an indispensable role in maintaining the electron density and initiating the final streamer-to-spark transition. When E/N reaches 50–75 Td, three-body attachment reactions are suppressed, the ozone are dissociated and electrons stored negative ions such as O^- , O_2^- and O_3^- , electrons can be released though collision with O-atoms to initiate the spark formation at the post discharge stage.

Spark stage is important because energy deposition rises in this stage, and the plasma is still chemically active before the equilibrium arc stage. The modeling methods proposed in this work make it possible to study streamer-spark discharges after gap closing in point-to-plane (and also point-to-point) configurations. The 2D–0D combined approach provides a self-consistent prediction. However, the ignition of sparks in the self-heated region due to previous discharges, which is a more general condition, is not studied in detail, and will be studied in the future by coupling with fluid dynamics.

Acknowledgments

The work was partially supported by the National Natural Science Foundation of China (No. 51907204, 51790511, 91941105, 91941301) and the National Numerical Windtunnel Project NNW2018-ZT3B08. The authors are thankful to the young research group in Atelier des Plasmas for fruitful discussions.

ORCID iDs

Xiancong Chen  <https://orcid.org/0000-0002-9924-7999>

Yifei Zhu  <https://orcid.org/0000-0001-8989-0051>

Yun Wu  <https://orcid.org/0000-0002-8575-0665>

References

- [1] Popov N A 2016 *Plasma Sources Sci. Technol.* **25** 043002
- [2] Adamovich I V and Lempert W R 2014 *Plasma Phys. Control. Fusion* **57** 014001
- [3] Yang S, Nagaraja S, Sun W and Yang V 2017 *J. Phys. D: Appl. Phys.* **50** 433001
- [4] Ju Y and Sun W 2015 *Prog. Energy Combust. Sci.* **48** 21–83
- [5] Starikovskaia S M 2014 *J. Phys. D: Appl. Phys.* **47** 353001
- [6] Li H-P, Ostrikov K K and Sun W 2018 *Phys. Rep.* **770–772** 1–45
- [7] Snoeckx R and Bogaerts A 2017 *Chem. Soc. Rev.* **46** 5805–63
- [8] Kozák T and Bogaerts A 2014 *Plasma Sources Sci. Technol.* **23** 045004
- [9] Lin B, Wu Y, Zhu Y, Song F and Bian D 2019 *Appl. Energy* **235** 1017–26
- [10] Sabzehparvar M, Kiani F and Tabrizi N S 2018 Spark discharge generation of superparamagnetic nickel oxide nanoparticles *Materials Today: Proc. INN Int. Conf./Workshop on Nanotechnology and Nanomedicine (NTNM2017)* (2–3 May 2017) vol 5 pp 15821–7
- [11] Asl M S, Nayebi B and Shokouhimehr M 2018 *Ceram. Int.* **44** 15269–73
- [12] Rocha L L, Silva J F and Redondo L M 2014 *IEEE Trans. Plasma Sci.* **42** 2956–61
- [13] Llewellyn-Jones F 1957 *Ionization and Breakdown in Gases* (London: Methuen)
- [14] Loeb L B and Meek J M 1941 *The Mechanism of the Electric Spark* (USA: Stanford University Press)
- [15] Meek J M 1940 *Phys. Rev.* **57** 722–8
- [16] Marode E, Bastien F and Bakker M 1979 *J. Appl. Phys.* **50** 140–6
- [17] Marode E 1975 *J. Appl. Phys.* **46** 2005–15
- [18] Morrow R and Lowke J J 1997 *J. Phys. D: Appl. Phys.* **30** 614–27
- [19] Naidis G V 1999 *J. Phys. D: Appl. Phys.* **32** 2649–54
- [20] Pai D Z, Lacoste D A and Laux C O 2010 *J. Appl. Phys.* **107** 093303
- [21] Janda M, Martišovič V and Machala Z 2011 *Plasma Sources Sci. Technol.* **20** 035015
- [22] Janda M, Machala Z, Niklová A and Martišovič V 2012 *Plasma Sources Sci. Technol.* **21** 045006
- [23] Janda M, Martišovič V, Hensel K, Dvonč L and Machala Z 2014 *Plasma Sources Sci. Technol.* **23** 065016
- [24] Janda M, Machala Z, Dvonč L, Lacoste D and Laux C O 2014 *J. Phys. D: Appl. Phys.* **48** 035201
- [25] Janda M, Martišovič V, Buček A, Hensel K, Molnár M and Machala Z 2017 *J. Phys. D: Appl. Phys.* **50** 425207
- [26] Janda M, Hoder T, Sarani A, Brandenburg R and Machala Z 2017 *Plasma Sources Sci. Technol.* **26** 055010
- [27] Tholin F and Bourdon A 2011 *J. Phys. D: Appl. Phys.* **44** 385203
- [28] Tholin F and Bourdon A 2013 *J. Phys. D: Appl. Phys.* **46** 365205
- [29] Zhu Y, Shcherbanev S, Baron B and Starikovskaia S 2017 *Plasma Sources Sci. Technol.* **26** 125004
- [30] Zhu Y and Starikovskaia S M 2018 *Plasma Sources Sci. Technol.* **27** 124007
- [31] Zhu Y, Wu Y, Wei B, Liang H, Jia M, Song H, Haojun X and Li Y 2019 *J. Phys. D: Appl. Phys.* **53** ab6517
- [32] Kulikovskiy A 1998 *Phys. Rev. E* **57** 7066
- [33] Pancheshnyi S, Eismann B, Hagelaar G and Pitchford L 2008 Computer code *zplaskin Tech. Rep.*, CNRS-UPS-INP University of Toulouse, Laplace www.zplaskin.laplace.univ-tlse.fr
- [34] Flitti A and Pancheshnyi S 2009 *Eur. Phys. J. Appl. Phys.* **45** 21001
- [35] Viehland L and Mason E 1995 *At. Data Nucl. Data Tables* **60** 37–95
- [36] Bourdon A, Pasko V, Liu N, Célestin S, Ségur P and Marode E 2007 *Plasma Sources Sci. Technol.* **16** 656–78
- [37] Luque A, Ebert U, Montijn C and Hundsdoerfer W 2007 *Appl. Phys. Lett.* **90** 081501

- [38] Zheleznyak M B, Mnatsakanian A K and Sizykh S V 1982 *High Temp. Sci.* **20** 423–8 <https://ui.adsabs.harvard.edu/abs/1982TepVT..20..423Z/abstract>
- [39] Tardiveau P, Moreau N, Bentaleb S, Postel C and Pasquiers S 2009 *J. Phys. D: Appl. Phys.* **42** 175202
- [40] Tarasenko V F, Naidis G V, Beloplotov D V, Kostyrya I D and Babaeva N Y 2018 *Plasma Phys. Rep.* **44** 746–53
- [41] Pechereau F, Le Delliou P, Jánský J, Tardiveau P, Pasquiers S and Bourdon A 2014 *IEEE Trans. Plasma Sci.* **42** 2346–7
- [42] Pechereau F 2013 Numerical simulation of the interaction of atmospheric pressure plasma discharges with dielectric surfaces *PhD Thesis Ecole centrale de Paris, Châtenay-Malabry*
- [43] Chng T L, Brisset A, Jeanney P, Starikovskaia S M, Adamovich I V and Tardiveau P 2019 *Plasma Sources Sci. Technol.* **28** 091t02
- [44] Raizer Y P 1991 *Gas Discharge Physics* (New York: Springer)
- [45] Sun S R, Kolev S, Wang H X and Bogaerts A 2016 *Plasma Sources Sci. Technol.* **26** 015003
- [46] Kolev S and Bogaerts A 2014 *Plasma Sources Sci. Technol.* **24** 015025
- [47] Sun S R, Kolev S, Wang H X and Bogaerts A 2017 *Plasma Sources Sci. Technol.* **26** 055017
- [48] Ramshaw J and Chang C 1993 *Plasma Chem. Plasma Process.* **13** 489–98
- [49] Hagelaar G J M and Pitchford L C 2005 *Plasma Sources Sci. Technol.* **14** 722–33
- [50] Zhu Y, Lepikhin N D, Orel I S, Salmon A, Klochko A V and Starikovskaia S M 2018 *Plasma Sources Sci. Technol.* **27** 075020
- [51] Flitti A and Pancheshnyi S 2009 *Eur. Phys. J. Appl. Phys.* **45** 21001
- [52] Kossyi I A, Kostinsky A Y, Matveyev A A and Silakov V P 1992 *Plasma Sources Sci. Technol.* **1** 207–20
- [53] Capitelli M, Ferreira C M, Gordiets B F and Osipov A I 2001 *Plasma Kinetics in Atmospheric Gases* vol 31 (Berlin: Springer)
- [54] Eichwald O, Ducasse O, Dubois D, Abahazem A, Merbahi N, Benhenni M and Yousfi M 2008 *J. Phys. D: Appl. Phys.* **41** 234002
- [55] Soloviev V R, Krivtsov V M, Shcherbanev S A and Starikovskaia S M 2016 *Plasma Sources Sci. Technol.* **26** 014001
- [56] Stepanyan S A, Soloviev V R and Starikovskaia S M 2014 *J. Phys. D: Appl. Phys.* **47** 485201
- [57] Montello A, Yin Z, Burnette D, Adamovich I V and Lempert W R 2013 *J. Phys. D: Appl. Phys.* **46** 464002
- [58] Shkurenkov I, Burnette D, Lempert W R and Adamovich I V 2014 *Plasma Sources Sci. Technol.* **23** 065003
- [59] Burnette D, Montello A, Adamovich I V and Lempert W R 2014 *Plasma Sources Sci. Technol.* **23** 045007
- [60] Shkurenkov I and Adamovich I V 2016 *Plasma Sources Sci. Technol.* **25** 015021
- [61] Naidis G V 1996 *J. Phys. D: Appl. Phys.* **29** 779–83
- [62] Tardiveau P, Marode E and Agneray A 2002 *J. Phys. D: Appl. Phys.* **35** 2823–9
- [63] Eyring C F, Mackeown S S and Millikan R A 1928 *Phys. Rev.* **31** 900–9
- [64] Celestin S 2008 Study of the dynamics of streamers in air at atmospheric pressure *PhD Thesis Ecole Centrale Paris*